CRYSTAL GROWTH & DESIGN

Article

pubs.acs.org/crystal

Co-Ligand Dependent Formation and Phase Transformation of Four Porphyrin-Based Cerium Metal−Organic Frameworks

Timo Rhauderwiek,[†] Niclas Heidenreich,[†,‡] Helge Reinsch,[†] Sigurd Øien-Ødegaard,[§] Kirill A. Lomachenko,[∥,⊥] Uta Rütt,[‡] Alexander V. Soldatov,[∥] Karl Petter Lillerud,[§] and Norbert Stock*[,†,§]

[†]Institut für Anorganische Chemie, Christian-Albrechts-Universität, Max-Eyth Straße 2, D-24118 Kiel, Germany

[‡]Deutsches-Elektronen-Synchrotron DESY, Notkestraße 85, 22607 Hamburg, Germany

[§]Department of Chemistry, University of Oslo, Sem Sælands vei 26, N-0371 Oslo, Norway

[∥]International Research Center "Smart Materials", Southern Federal University, Zorge Street 5, 344090 Rostov-on-Don, Russia

[⊥]European Synchrotron Radiation Facility, 71 avenue des Martyrs, CS 40220, 38043 Grenoble Cedex 9, France

Supporting Information

ABSTRACT: The four porphyrin-based metal−organic frameworks (MOFs) containing Ce^{3+} ions, $[Ce_4(H_2TCPP)_3(DMF)_2(H_2O)_4]$ (**CAU-18**), $[Ce_4(H_2TCPP)_3]\cdot 22H_2O$ (**CAU-18a**), $[Ce_3(H_2TCPP)_2(BA\text{-}X)(HBA\text{-}X/H_2O)_2]\cdot 2HBA\text{-}X\cdot nH_2O$ (**CAU-19-X** with X = H, 2Cl, 3Cl, 4Cl, $3CO_2H$, $4NH_2$, $4NO_2$, HBA = $C_7H_4O_2$), and $[Ce_2(H_2TCPP)(C_7H_4O_2NO_2)_2]\cdot 2DMF$ (**Ce-PMOF-4NO$_2$**) were synthesized using the linker 4-tetracarboxyphenylporphyrin (H_6TCPP). The formation of the respective MOFs depends mainly on the presence of a coligand in the synthesis mixture. **CAU-18** was obtained in the absence of a coligand, while **CAU-19-X** was observed when the benzoic acid derivative HBA-X (X = H, 2Cl, 3Cl, 4Cl, $3CO_2H$, $4NH_2$) was added. In the case that HBA-$4NO_2$ was used as a coligand, yet another compound **Ce-PMOF-4NO$_2$** is obtained. The structures of **CAU-18** and **CAU-19-H** were determined from single crystal X-ray diffraction data, while the structure of **Ce-PMOF-4NO$_2$** was refined from powder X-ray diffraction data by the Rietveld method. Activation of **CAU-18** and **Ce-PMOF-4NO$_2$** resulted in phase transformations. Thermal treatment of **CAU-18** at 250 °C leads to **CAU-18a**, which is porous toward N_2 and H_2O, while treatment of **Ce-PMOF-4NO$_2$** in organic solvents at 70 °C leads to the formation of **CAU-19-4NO$_2$**, which cannot be synthesized directly. All **CAU-19-X** compounds are porous toward N_2 and H_2O, and the specific surface areas vary between 330 and 600 $m^2\ g^{-1}$ depending on the size of the incorporated coligand. **CAU-18**, **CAU-18a**, and **CAU-19-X** are thermally stable in air up to 330 °C and chemically stable in H_2O and all tested organic solvents. Ce L_3-edge X-ray absorption near edge structure measurements revealed that exclusively Ce^{3+} ions are present in the title compounds, despite the use of $(NH_4)_2[Ce(NO_3)_6]$ in all syntheses. In addition, the crystallization of **CAU-18** and **CAU-19-H** was investigated in situ by synchrotron powder X-ray diffraction at DESY, Hamburg, using reaction temperatures between 110 and 130 °C. The data were evaluated using the approach by Gualtieri to determine the probability of nucleation (P_n) and the Arrhenius activation energy for nucleation (k_n) and crystal growth (k_g). The Arrhenius activation energies for the nucleation were determined as 47(2) and 56(3) kJ mol^{-1} and for crystal growth 45(4) and 58(5) kJ mol^{-1} for **CAU-18** and **CAU-19-H**, respectively. The induction time (t_{ind}), in which no crystalline products are detected, and the total reaction time to achieve full conversion (t_{com}) are shortened at higher temperatures. Furthermore, the maximum of the probability of nucleation is shifted to earlier reaction times with increasing temperature.

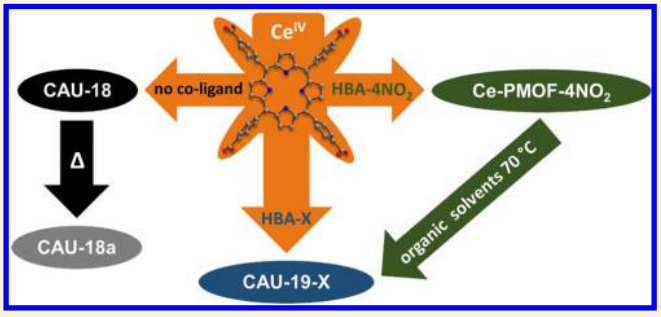

INTRODUCTION

The modular structure of metal−organic frameworks (MOFs) allows one to tune the pore size and pore surface properties, which in turn leads to a large range of chemical and physical properties.[1−4] Hence MOFs have been investigated in applications such as gas storage and separation, drug delivery, or catalysis.[1,3,5−7] In situ crystallization investigations were performed in recent years to study crystallization processes of MOFs in solution and to determine kinetic parameters. Examples comprise the formation of MIL-53[8] and MIL-100,[9] which are formed through an intermediate crystalline phase, MOF-14,[10] which starts to decompose at longer reaction times, and CAU-1,[11] which was shown quantitatively to form within a few minutes.[12]

Porphyrin-based linker molecules have been intensively investigated in the synthesis of MOFs since the resulting porphyrin-based MOFs are often redox active. They have been used in catalysis[13−21] and were also tested for the singlet

Received: March 28, 2017
Revised: May 3, 2017
Published: May 8, 2017

DOI: 10.1021/acs.cgd.7b00450
Cryst. Growth Des. 2017, 17, 3462−3474

oxygen production in biomedical and nonmedical applications as well as cancer therapy.[22−24] MOFs containing tri- or tetravalent cations are known for their high stability,[25] and in combination with 4-tetracarboxyphenylporphyrine (H_6TCPP), which is the most intensively investigated porphyrin-linker in MOF synthesis,[26−28] various compounds exhibiting permanent porosity have been reported. First pioneering work in the field of porphyrin-based MOFs incorporating the H_6TCPP ligand were carried out by Suslick et al. and Goldberg et al. in 2000 and 2002.[29,30] More recent studies led to Zr-MOFs known as PCN-221 to -225,[13,31,14,32] MOF-545,[33] and MOF-525.[33,34] Some of these compounds have been tested in various catalytic reactions, such as the oxidation of cyclohexane,[35] the electrochemical reduction of CO_2,[16] or the photooxidation of mustard gas.[19] A larger variety of porphyrin-based MOFs are known with trivalent ions. Thus, three isoreticular MOFs with the group 13 metal ions aluminum, gallium, and indium (Al-PMOF,[36] Ga-PMOF,[37] In-PMOF)[37] have been reported, and the Al-PMOF was investigated in the photocatalytic methyl viologen assisted H_2-generation on colloidal platinum.[36] In addition, porphyrin-based In-MOFs (MMPF-7,[38] MMPF-8,[38] and UNLPF-10[39,40]), Fe-MOFs (MIL-141,[41] [Fe_2(Fe-TCPP)-($C_4H_4N_2$) (OH_2)]) ($C_4H_4N_2$ = pyrazine),[42] and PCN-600)[43] and MOFs containing lanthanide ions like Ce,[44,45] Nd,[46] Sm,[47] and Dy[46] are also known. For the latter examples, only the crystal structures but no physisorption measurements were reported.

Herein we present the results of our systematic investigation on the synthesis of 12 trivalent Ce-MOFs using the porphyrin-based linker H_6TCPP in the absence and presence of various benzoic acid derivatives (HBA-X, X = H, Cl, NH_2, NO_2, COOH) that can act as a coligand (Figure 1), their structural transformation upon activation as well as the results of our in situ crystallization studies.

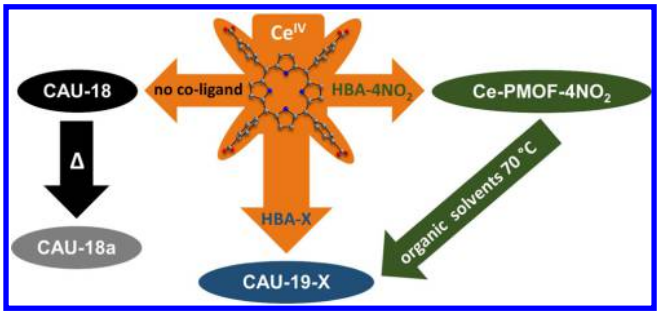

Figure 1. Graphical representation of the investigation of the system Ce^{4+}/H_6TCPP/DMF/H_2O in the absence or presence of benzoic acid derivatives (HBA-X, X = H, Cl, NH_2, NO_2, COOH) as coligands. The study led to the new porphyrin-based Ce-MOFs **CAU-18**, **CAU-18a**, **CAU-19-X** (X = H, 2Cl, 3Cl, 4Cl, 4NH_2, 4NO_2, 3CO_2H) and **Ce-PMOF-4NO_2**.

EXPERIMENTAL SECTION

Materials. Cerium(IV) ammonium nitrate ($(NH_4)_2[Ce(NO_3)_6]$) (98%, ABCR), benzoic acid (99.5%, ABCR), 2-chlorobenzoic acid (98%, ABCR), 3-chlorobenzoic acid (99%, Sigma-Aldrich), 4-chlorobenzoic acid (99%, Sigma Alrich), 3-carboxybenzoic acid (trimellitic acid, 99%, Sigma-Aldrich), 4-aminobenzoic acid (99%, Sigma-Aldrich), 4-nitrobenzoic acid (99%, ABCR), $ZnSO_4 \cdot H_2O$ (97%, Merck), $CoCl_2 \cdot 6\ H_2O$ (98%, Fluka), dimethylformamide (DMF, 99%, Grüssing), aceton (99%, Walther), methanol (99%, Walther), dichloromethane (DCM, 99%, Walther), and ethanol (99%, Walther) were used without further purification. The cerium(IV) ammonium nitrate was dissolved in distilled H_2O to achieve a 0.53 M solution. The linker 4,4′,4″,4‴-(5,10,15,20-porphyrintetrayl)tetrabenzoic acid (4-tetracarboxyphenylporphyrin, H_6TCPP) was synthesized according to reported procedures[48−50] starting with 4-formylbenzoic acid (98%, ABCR) and pyrrole (98%, ABCR) in propionic acid (99%, Grüssing). The metalated linker Co-H_4TCPP was synthesized according to reported procedures. First Co-TCPP-Me_4[51] was obtained by reaction of H_6TCPP with $CoCl_2 \cdot 6H_2O$ in MeOH which was subsequently hydrolyzed.[52] Details are given in the Supporting Information.

Characterization. Single crystal X-ray diffraction data for **CAU-18** and CAU-19-H were acquired at the beamline ID11 at ESRF (Grenoble, France). The reflections were indexed with the APEX3 suite, integrated with SAINT V9.32B,[53] solved with the program SHELXL,[54] and refined with the program SHELXL using Olex2 as GUI.[55] A radiation energy of 40 keV was used, corresponding to a wavelength of λ = 0.3112 Å. The nonstandard wavelength induced a checkcif warning due to mismatch of the determined and calculated absorption coefficient μ. Only one full hemisphere (ϕ scan) was collected for each sample, due to time constraints, resulting in incomplete data sets. Both crystals were very small and poorly diffracting, and in addition suffered from radiation damage during the measurements. Both structures contain stacked porphyrin rings, likely to cause stacking disorder in the crystals. This disorder is likely to have caused the poor precision on bond lengths and ADP values in the obtained crystal structures. Restraints forcing ADP tensor components to approximate to isotropic behavior (isor) and rigid body restraints (rigu) were used to prevent unphysical ADP values.

All Ce L_3-edge X-ray absorption near edge structure (XANES) measurements, except for $Ce(NO_3)_3 \cdot 6\ H_2O$, were performed at the Southern Federal University (Rostov-on-Don, Russia) using a Rigaku R-XAS spectrometer. The water-cooled X-ray tube with a fixed W anode was operating at 12 kV and 80 mA. The incident beam was monochromatized using a Johansson-type Ge (220) crystal, ensuring an energy resolution of around 1 eV at Ce L_3-edge (5730 eV). The measurements were conducted in transmission mode using an Ar-filled ionization chamber and a scintillation counter to monitor the intensity of incident (I_0) and transmitted (I_1) radiation, respectively. A He-filled bag was placed between the X-ray tube, the monochromator, and the I_0 detector to reduce the X-rays absorption in air. The spectrum of $Ce(NO_3)_3 \cdot 6\ H_2O$ was collected at the BM23 beamline of the European Synchrotron Radiation Facility (Grenoble, France) in transmission mode using a Si (111) crystal for monochromatization, Si mirrors for harmonics rejection and N_2/He-filled ionization chambers for photon detection, yielding resolution comparable with the laboratory measurement. In all cases the samples were measured in the form of self-supporting pellets mixed with boron nitride and pressed with a pressure below 400 kg/cm^2. Mass of the samples was optimized by using the XAFSmass code[56] to obtain the best signal-to-noise ratio.

Powder X-ray diffraction (PXRD) measurements were carried out with a STOE HT diffractometer equipped with a xy-stage and an IPDS (Cu $K_{\alpha 1}$ radiation) or Mythen (Mo $K\alpha_1$ radiation) detector system. High resolution PXRD patterns were measured on a STOE Stadi-P combi powder diffractometer equipped with a Mythen detector (Cu $K\alpha_1$ radiation). The structure of **Ce-PMOF-4NO_2** was refined from PXRD data using the Rietveld method. Only an approximated structure model was obtained due to broad reflections with a low signal-to-noise ratio and the presence of small amounts of **CAU-19-4NO_2**. An appropriate structure model for **CAU-18a** could not be set up due to limited long-range order in the sample. Nevertheless, the PXRD pattern of **CAU-18a** could be indexed using TOPAS academic V4.1,[57] and a unit cell similar to **CAU-18** was found and confirmed by a Pawley fit (Table 2 and Figure S20). Pawley fits (Figures S22−S29) were carried out for all other **CAU-19-X** and **M-CAU-19-H** (M = Zn, Co) derivatives to proof that they are isostructural to **CAU-19-H**. Pawley fits of **CAU-18** and **CAU-19-H** (Figures S19 and S21) with the lattice parameters determined from the single crystal structure determination were carried out to prove the phase purity. Pawley fits and Rietveld-refinements were performed with the program

DOI: 10.1021/acs.cgd.7b00450
Cryst. Growth Des. 2017, 17, 3462−3474

Table 1. Summary and Comparison of the Synthesis Parameters of CAU-18, CAU-19-X (X = H, 2Cl, 3Cl, 4Cl, $3CO_2H$, $4NH_2$), and Ce-PMOF-$4NO_2$[a]

CAU	-18	-19-H	-19-Cl[b]	-19-$4NH_2$	-19-$3CO_2$	Ce-PMOF
M/L/HBA-X[c]	1:2:0	1:2:180	1:2:150	1:2:200	1:2:140	9:18:450
H_2O/DMF[d]	1:3	1:3	1:3	1:3	1:3	2.8:30
HBA-X [mg]		570	600	700	600	2000
T [°C]	100	120	120	120	120	120
t [h]	2	24	2	24	24	48
yield [%]	79	56	51, 30, 72[b]	75	37	44

[a]All **CAU-19-Cl** derivatives were obtained using the same synthesis parameters. All syntheses were carried out in 7 mL glass vials except **Ce-PMOF-4NO$_2$**, which was synthesized in a 30 mL Teflon reactor. [b]**CAU-19-Cl** indicates all **CAU-19-Cl** derivatives in following order 2Cl, 3Cl, 4Cl. [c]Molar ratio, the number 1 corresponds to 2.53×10^{-2} (20 mg) mmol. [d]Volumetric ratio, the number 1 corresponds to 300 μL of H_2O.

TOPAS academic V4.1.[57] The results of the refinement and crystallographic data of **CAU-18**, **CAU-18a**, **CAU-19-H**, and **Ce-PMOF-4NO$_2$** is shown in Table 2. The refined cell parameters and results of the Pawley fits of the other **CAU-19-X** and **M-CAU-19-H** (M = Zn, Co) derivatives are shown in Tables S2 and S3 and Figures S19–S29. The diameters of all pores were determined using DIAMOND V.3[58] taking the van-der-Waals radii of the atoms into account. The variable temperature PXRD (VT-PXRD) measurements were recorded on a STOE Stadi-P combi powder diffractometer (Cu Kα_1 radiation: **CAU-18**; Mo Kα_1 radiation: **CAU-19-H**) equipped with a capillary furnace. For the measurements 0.5 mm quartz capillaries were used. The samples were heated up in steps of 5 K to 500 and 600 °C for **CAU-18** and **CAU-19-H**, respectively, and measured for 10 min each.

The in situ PXRD measurements were carried out at beamline P09[59] (λ = 0.53905 Å) and P07B[60] (λ = 0.14235 Å) at PETRA III, DESY, Hamburg. The sample-to-detector distance was 606.074 mm and 2682.568 mm at P09 and P07B, respectively. In both cases a PerkinElmer 1621 flat panel detector (2048 × 2048 pixel; 200 μm × 200 μm pixel size) was used. At beamline P09,[59] the experiments were executed with a beam size of 1 × 1 mm. At beamline P07B,[60] the beamsize was set to 0.5 × 0.5 mm. The reactions were carried out in a custom-built reactor that was developed at CAU Kiel in cooperation with the beamline staff of beamline P08, PETRA III, DESY.[61] The reactor was designed to enable the analysis of chemical reactions under solvothermal reaction conditions via synchrotron based techniques. The core of the reactor consists of an aluminum casing surrounded by copper-galvanized heating wires. Reaction vessels made from borosilicate glass (V_{max} = 5 mL) can be inserted into the casing that is aligned in transmission geometry on the beamline. The temperature inside the reaction vessel was constantly monitored throughout the entire reaction by means of a PTFE-coated k-type thermocouple. Through a combination of resistive heating from the heating wires and direct cooling of the heating wires via compressed air the temperature inside, the glass vessel was precisely controlled with a deviation of ±0.5 °C. A stirring device under the base of the reactor allowed for homogenization of the sample during the reaction. The setup furthermore provides the option of adding solutions during the reaction by means of a remote-controlled syringe pump. The syringe pump system is connected to PTFE tubes that are embedded in the custom-built screw caps. In this study the syringe pump was used to start the reactions remotely that lead to the formation of **CAU-19-H**. To ensure a constant reaction temperature the linker solution was first heated to the target temperature followed by the injection of metal salt solution to start the reaction. A more detailed description of the experiment procedure is provided in the section discussing the in situ studies.

IR spectra were recorded using a Bruker ALPHA-FT-IR A220/D-01 spectrometer equipped with an ATR unit. UV/vis spectra were recorded at a Spectroquant Pharo 300 M. Prior to the measurements all samples were dissolved in 2 M NaOH and measured at once. ^{1}H NMR spectroscopy was employed for the quantitative analysis of occluded guest molecules and coligands. The NMR spectra were recorded on a Bruker DRX 500 spectrometer. The samples were dissolved in a mixture of 10% deuterochloric acid (DCl) in D_2O and deuterated dimethyl sulfoxide (DMSO-d_6) (molar ratio = 1:7). Sorption experiments were performed with a BEL Japan Inc. BELSORP-max. Before sorption measurements all samples were activated at 170 °C under reduced pressure (10^{-2} kPa) for 16 h. Thermogravimetric measurements were performed on a NETZSCH STA 409 CD analyzer under a flow of air (75 mL min^{-1}) with a heating rate of 4 °C min^{-1} between 25 and 700 °C in Al_2O_3-crucibles. The data were corrected for buoyancy and current effects.

Preparation. The syntheses of **CAU-18** and **CAU-19-X** (X = H, 2Cl, 3Cl, 4Cl, $3CO_2H$, $4NH_2$, $4NO_2$) were carried out in glass vials (V_{max} = 7.0 mL, Pyrex) using a solvent mixture (volume ratio H_2O to DMF of 1 to 3). **Ce-PMOF-4NO$_2$** was obtained in 30 mL autoclaves with Teflon inserts using DMF as solvent and 4-nitrobenzoic acid as coligand. For the synthesis optimization reactions were carried out between 80 and 140 °C, at reaction times between 1 and 48 h using different molar ratios of metal/linker/HBA-X between 1:1:0 and 5:1:300 (HBA-X = $C_7H_5O_2$-X, X = X = H, 2Cl, 3Cl, 4Cl, $3CO_2H$, $4NH_2$, $4NO_2$). The formation of the metalated compounds **M-CAU-19-H** (M = Zn, Co) was investigated starting from the synthesis conditions of **CAU-19-H**. In the case of **Zn-CAU-19-H** the addition of $ZnSO_4 \cdot H_2O$ and a reaction time of 1 h resulted in the formation of **Zn-CAU-19-H**. **Co-CAU-19-H** was obtained by an increase of metal to linker ratio to 5:1 and a higher amount of DMF (2400 μL). Activation of the samples was carried out by thermal treatment or by a combination of solvent exchange at elevated temperatures followed by thermal treatment under reduced pressure.

The optimized synthesis parameters of all title compounds are summarized in Table 1, and the results of the elemental analyses are given in Table S1. The detailed synthesis procedures for **CAU-18**, **CAU-18-HT**, **CAU-19-H**, **M-CAU-19-H** (M = Zn, Co) and **Ce-PMOF-4NO$_2$** are as follows.

CAU-18. H_6TCPP (20 mg, 2.53×10^{-2} mmol), DMF (1200 μL), H_2O (300 μL), and 0.53 M aqueous $(NH_4)_2[Ce(NO_3)_6]$ solution (94 μL, 5.06×10^{-2} mmol) were added to a 7.0 mL glass vial. The glass vial was heated for 2 h at 100 °C. The resulting product was filtered off and washed two times each with DMF and acetone. A yield of 63 mg (79% based on H_6TCPP) was obtained for **CAU-18**, $[Ce_4(H_2TCPP)_3(DMF)_2(H_2O)_4]$.

CAU-18a. **CAU-18** (500 mg, 0.16 mmol) was placed in a crucible and heated for 24 h at 250 °C. A yield of 470 mg, 100% was obtained for **CAU-18a**, based on the composition $[Ce_4(H_2TCPP)_3] \cdot 22\ H_2O$ deduced from elemental analysis and thermogravimetric (TG) measurements.

CAU-19-H. H_6TCPP (20 mg, 2.53×10^{-2} mmol), benzoic acid (HBA-H) (570 mg, 4.67 mmol), DMF (1200 μL), H_2O (300 μL), and 0.53 M aqueous $(NH_4)_2[Ce(NO_3)_6]$ solution (94 μL, 5.06×10^{-2} mmol) were added to a 7.0 mL glass vial. The glass vial was heated for 24 h at 120 °C. The resulting product was filtered off and washed two times each with DMF and acetone. A yield of 16 mg, 56% (based on H_6TCPP) was obtained for CAU-19-H, $[Ce_3(H_2TCPP)_2(BA\text{-}H)(HBA\text{-}H/H_2O)_2] \cdot 2(HBA\text{-}H) \cdot 11H_2O$.

Zn-CAU-19-H. H_6TCPP (20 mg, 2.53×10^{-2} mmol), $ZnSO_4$ (5 mg, 3.10×10^{-2} mmol), benzoic acid (HBA-H) (570 mg, 4.67 mmol), DMF (1200 μL), H_2O (300 μL), and 0.53 M aqueous $(NH_4)_2[Ce(NO_3)_6]$ solution (94 μL, 5.06×10^{-2} mmol) were added to a 7.0 mL

DOI: 10.1021/acs.cgd.7b00450
Cryst. Growth Des. 2017, 17, 3462–3474

Table 2. Crystallographic Data of CAU-18, CAU-18a, CAU-19-H, and Ce-PMOF-4NO$_2$

	CAU-18	CAU-18a	CAU-19-H	Ce-PMOF-4NO$_2$
formula	$[Ce_4(H_2TCPP)_3(DMF)_2(H_2O)_4]$	$[Ce_4(H_2TCPP)_3]$	$[Ce_3(H_2TCPP)_2(C_7H_4O_2H)_2(H_2O)_2]$	$[Ce_2(H_2TCPP)(C_7H_4O_2NO_2)_2]$
data determined by	single crystal	Pawley fit	single crystal	Rietveld refinement
crystal system	monoclinic	monoclinic	triclinic	orthorhombic
a [Å]	20.755(5), 23.572(6), 30.642(8)	22.420(3)	11.665(7)	33.077(3)
b [Å]		23.248(3)	13.915(8)	7.309(2)
c [Å]		34.419(5)	17.343(10)	16.539(2)
α [°]	90	90	95.514(4)	90
β [°]	104.573 (2)	106.375(5)	99.792(4)	90
γ [°]	90	90	101.313(5)	90
V [Å^3]	14509(7)	17212(4)	2696(3)	3998(1)
space group	$C2/c$	$P2/c$	$P\bar{1}$	$Cmmm$
tot., uniq. data, R_{int}	21207, 12183, 0.073		10313, 9008 0.038	
observed data [$I > 2\sigma(I)$]	6622		6710	
R_1, wR_2 (gt) [%]	7.5, 18.0		7.8, 20.6	
GOF	0.97	1.19	1.04	1.24
R_{wp}		2.03		4.46

glass vial. The glass vial was heated for 1 h at 120 °C under stirring. The resulting product was filtered off and washed two times each with DMF and acetone. A yield of 15 mg, 53% (based on H_6TCPP) was obtained for **Zn-CAU-19-H**, $[Ce_3(Zn\text{-}TCPP)_2(BA\text{-}H)(HBA\text{-}H/H_2O)_2]\cdot 2(HBA\text{-}H)\cdot 8H_2O$.

Co-CAU-19-H. Co-H_4TCPP (20 mg, 2.53×10^{-2} mmol), benzoic acid (HBA-H) (570 mg, 4.67 mmol), DMF (2400 μL), H_2O (350 μL), and 0.53 M aqueous $(NH_4)_2[Ce(NO_3)_6]$ solution (94 μL, 12.65×10^{-2} mmol) were added to a 7.0 mL glass vial. The glass vial was heated for 2 h at 120 °C under stirring. The resulting product was filtered off and washed two times each with DMF and acetone. A yield of 12 mg, 42% (based on Co−H_4TCPP) was obtained for Co-CAU-19-H, $[Ce_3(Co\text{-}TCPP)_2(BA\text{-}H)(HBA\text{-}H/H_2O)_2]\cdot 2(HBA\text{-}H)\cdot 11H_2O$.

To prove that the porphyrin linker is still metalated after the MOF synthesis UV/vis spectra (Figure S4) were measured. Prior to the measurements all samples were dissolved in 2 M NaOH. The measurements reveal no significant loss of Co^{2+} and Zn^{2+} ions. The absorption maxima of the linker molecules incorporated in **CAU-19-H**, **Zn-CAU-19-H**, and **Co-CAU-19-H** after dissolution in 2 M aqueous NaOH solution were observed at 414, 422, and 430 nm, respectively, and correspond well to values reported in the literature (H_6TCPP = 413,[18,62] Zn-H_4TCPP = 424 nm,[63] Co-H_4TCPP = 430 nm[18]).

To remove the noncoordinating solvent and HBA-X molecules from the as-synthesized samples, the materials were treated under reflux with acetone (**CAU-19-X**, with X = H, 2Cl, 4Cl, 4NH_2, and **M-CAU-19-H** (M = Zn, Co)) or DMF (**CAU-19-3Cl** and **CAU-19-3CO$_2$H**). This procedure was repeated until no further decrease of the amount of HBA-X was observed in the ^{1}H NMR spectra (Figures S5−S12).

Ce-PMOF-4NO$_2$. H_6TCPP (180 mg, 22.77×10^{-2} mmol), 4-nitrobenzoic acid (HBA-4NO_2) (2000 mg, 12.05 mmol), DMF (9000 μL), and 0.53 M aqueous $(NH_4)_2[Ce(NO_3)_6]$ solution (850 μL, 45.54×10^{-2} mmol) were added to a 30 mL Teflon vessel. The Teflon vessel was placed in an autoclave and was heated for 48 h at 120 °C. The resulting product was filtered off and washed with 100 mL DMF. A yield of 139 mg, 44% (based on H_6TCPP) was obtained for **Ce-PMOF-4NO$_2$**, $[Ce_2(H_2TCPP)(BA\text{-}4NO_2)_2]\cdot 2DMF$.

CAU-19-4NO$_2$. **Ce-PMOF-4NO$_2$** (500 mg, 0.36 mmol) and 30 mL of acetone were placed in a 50 mL glass vessel with screw cap and heated in an oven for 72 h at 70 °C. A yield of 427 mg, 100% was obtained for **CAU-19-4NO$_2$** (yield calculated based on the linker molecule and corresponding to the formula $[Ce_3(H_2TCPP)_2(BA\text{-}NO_2)(HBA\text{-}NO_2/H_2O)_2]\cdot 2(HBA\text{-}NO_2)\cdot 6H_2O$ for **CAU-19-4NO$_2$**).

RESULTS AND DISCUSSION

The systematic study employing the linker molecule 4-tetracarboxyphenylporphyrine (H_6TCPP) as well as coligands (HBA-X, with X = X = H, 2Cl, 3Cl, 4Cl, 3CO_2H, 4NH_2, 4NO_2) led to 12 new porphyrin-based Ce-MOFs. In contrast to previous studies in the Goldberg group, we used coligands in our syntheses which have a strong influence on the product formation.[45]

The synthesis of the porphyrin-based Ce-MOFs was investigated starting from the reaction procedures recently reported for the synthesis of Ce-UiO-66 and an In-MOF containing the H_2TCPP^{4-} ion.[21,37] The title compounds **CAU-18**, $[Ce_4(H_2TCPP)_3(DMF)_2(H_2O)_4]$ and **CAU-19-X**, $[Ce_3(H_2TCPP)_2(BA\text{-}X)(HBA\text{-}X/H_2O)_2]\cdot 2HBA\cdot 11H_2O$, were obtained under very similar reaction conditions as described for the formation of Ce-UiO-66.[21] Thus, $(NH_4)_2[Ce(NO_3)_6]$ was used as the metal source, and the reaction was carried out using short reaction times (T_{max} = 2 h), low reaction temperatures (100−120°), and a DMF/H_2O solvent mixture (3:1). Although the formation of a hexanuclear $\{Ce_6O_8\}$ cluster and therefore the crystallization of compounds isostructural to the known porphyrin-based Zr-MOFs[34] were anticipated, this approach resulted in the formation of new Ce-MOFs with dimeric and trimeric IBUs that are connected by the H_2TCPP^{4-} ions to form three-dimensional framework structures. **CAU-18** is formed in the absence of a coligand, while **CAU-19-H** was obtained in the presence of benzoic acid (HBA). Subsequently, usage of different benzoic acid derivatives (HBA-X, with (X = H, 2Cl, 3Cl, 4Cl, 3CO_2H, 4NH_2) resulted in the formation of a series of CAU-19 type compounds with the BA-X$^-$ ions incorporated into the crystal structure. While the molar ratio Ce^{4+} to H_6TCPP has the most pronounced impact on the product formation, the amount of coligand varies slightly (Table 1). Unexpectedly, the use of 4-nitrobenzoic acid (HBA-NO_2) as a coligand and the increase of the DMF to H_2O ratio from 3:1 to 9:1 result in the formation of the new Ce-MOF $[Ce_2(H_2TCPP)(BA\text{-}4NO_2)_2]\cdot 2DMF$ (**Ce-PMOF-4NO$_2$**).

Activation of the Ce-MOFs. Thermal activation and VT-PXRD measurements of the title compounds revealed several structural changes. Thus, the thermal treatment of **CAU-18** at 250 °C leads to a desolvated compound denoted **CAU-18a**. Activation of **Ce-PMOF-4NO$_2$** was carried out in a two-step

DOI: 10.1021/acs.cgd.7b00450
Cryst. Growth Des. 2017, 17, 3462−3474

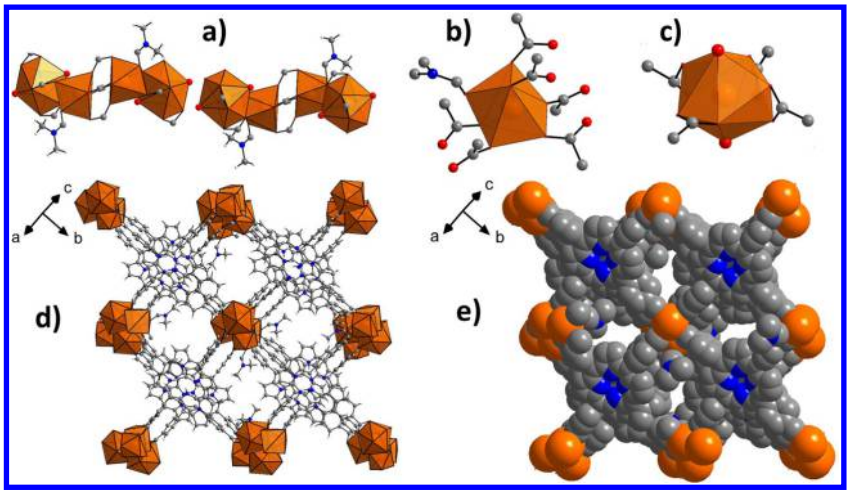

Figure 2. Structure of **CAU-18**. (a) IBUs composed of edge-sharing CeO_7 and CeO_9 polyhedra with bridging $-COO^-$ groups and coordinated DMF and water molecules, (b) CeO_7 polyhedron and coordination environment, (c) CeO_9 polyhedron and coordination environment, (d) view of the framework structure, (e) space filling model of **CAU-18**. Carbon atoms are shown in gray, oxygen atoms in red, nitrogen atoms in blue, and cerium atoms/CeO polyhedra in orange.

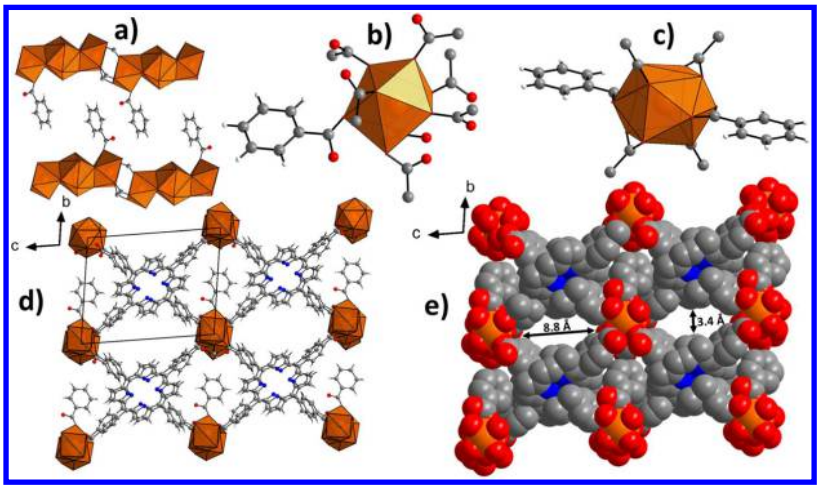

Figure 3. (a) IBU of **CAU-19-H** along [010], (b) CeO_8 polyhedron and coordination environment, (c) CeO_{12} polyhedron and coordination environment, (d) view along pores [100] with unit cell edges, and (e) space filling model along [100] of **CAU-19-H** with pore diameters of 3.4/8.8 Å. Carbon atoms are shown in gray, oxygen atoms in red, nitrogen atoms in blue, and cerium atoms/CeO polyhedra in orange.

process by treatment with an organic solvent at elevated temperatures, followed by thermal treatment under reduced pressure. The first step leads to the transformation of **Ce-PMOF-4NO$_2$** into **CAU-19-4NO$_2$** within 72 h at 70 °C. It is noteworthy that we have only been able to obtain **CAU-19−4NO$_2$** by this treatment.

Crystal Structure. The title compounds **CAU-18** and **CAU-19-H** were obtained as single crystals (Figures S13 and S14), while all other MOFs were only synthesized as microcrystalline powders. Hence the structures of **CAU-18** and **CAU-19-H** were determined from single crystal X-ray diffraction data, while the one of **Ce-PMOF-4NO$_2$** was refined from PXRD data (Figure 5, Table 2). In addition Pawley fits were carried out to determine the lattice parameters and to confirm phase purity of all title compounds (Figures S19−S29, Tables S2−S3).

CAU-18 is isostructural to $[Sm_4(H_2TCPP)_3(DMF)_2(H_2O)_4]$.[47] The IBU consists of edge-sharing CeO_7 and CeO_9 polyhedra, in a monocapped trigonal prismatic and a distorted tricapped trigonal prismatic coordination environment (Figure 2). Each CeO_7 polyhedron contains one DMF molecule and each CeO_9 polyhedron two water molecules, and the other oxygen atoms stem from carboxylate groups. The dimers are bridged to tetramers by carboxylate groups (Figure 2), and further interconnection by H_2TCPP^{4-} ions leads to a three-dimensional framework with very small pores of 2.4 × 5.0 Å, which are too small to accommodate guest molecules (Figure 2). Adjacent tetramers approach each other along [101] to a distance of 3.13(3) Å, which hints at the presence of a weak H-bond interaction between a coordinated water molecule and an oxygen atom of a carboxylate group (Figure S15). The coordination modes of the carboxylate groups in CAU-18 are shown in Figure S16 using the Harris notation.[64] The Harris notation has the format [A,XY], the value A is the number of metal ions coordinated by the carboxylate group, and X, Y is the number of bonds every oxygen shares with a metal ion.[64] In the structure of **CAU-18** the coordination modes [2,21], [2,11], [1,11], and [1,10] are observed.

The bond lengths found in **CAU-18** are in good agreement with the literature values. For the Ce−O bonds values between 2.296(10) (CN: 7) and 2.841(7) Å (CN: 9) were found which are in good agreement with the literature value of 2.386(8)

DOI: 10.1021/acs.cgd.7b00450
Cryst. Growth Des. 2017, 17, 3462−3474

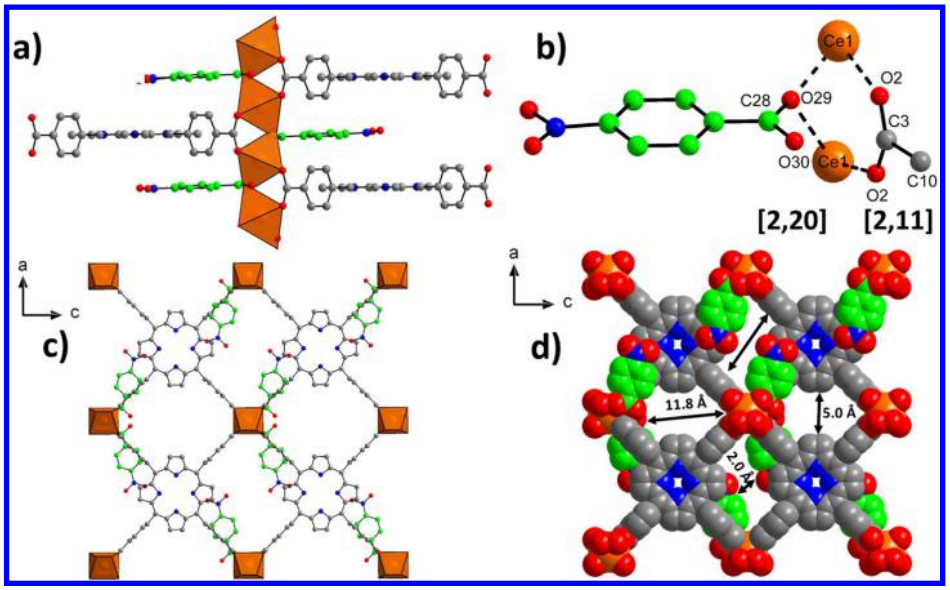

Figure 4. Structure of **Ce-PMOF-4NO$_2$**. (a) IBU along [100] with BA-NO$_2^-$ ions as bridging groups between trans corner-sharing CeO$_6$ polyhedra (b) Harris notation in brackets for the carboxylate group of the coligand and the linker, (c) view along pores [010], and (d) space filling model along [010] with pore diameters of 5.0 × 11.8 Å and 2.0 × 11.8 Å, respectively. Carbon atoms are shown in gray, oxygen atoms in red, nitrogen atoms in blue, and cerium atoms/CeO polyhedra in orange; for clarity the carbon atoms of the BA-NO$_2^-$ ion are marked in green.

(CN:7) and 2.797(7) Å (CN:9).[45,65] The C═C double bond length varies between 1.319(14) (arom. phenyl) and 1.481(11) Å (arom. pyrrole) and the N═C double bond length between 1.323(12) and 1.349(10) Å, which are also in good agreement with the literature values of 1.303(9) to 1.508(6) Å and 1.358(6) to 1.383(6) Å, respectively.[33,45]

CAU-19, [Ce$_3$(H$_2$TCPP)$_2$(BA-X)(HBA-X/H$_2$O)], can be synthesized with different benzoic acid derivatives (HBA-X, X = H, 2Cl, 3Cl, 4Cl, 4NH$_2$, 3CO$_2$H) which are part of the structure (Figure 3). The IBU contains trimers which are formed by edge-sharing of two CeO$_8$ and one CeO$_{12}$ polyhedra, in a distorted square antiprismatic and a distorted icosahedral coordination environment.

The coligands are incorporated as the benzoic acid derivative ([1,10] mode) as well as the anion ([1,11] mode) (Figure 3b,c)). The trimeric IBUs are connected to chains along [100] by H$_2$TCPP^{4-} ions (Figure 3), which also connect the chains to a three-dimensional framework structure with linear oval channels along [100]. These pores have diameters of 3.4 × 8.8 Å and are accessible to guest molecules (Figure 3). In the as-synthesized compounds the pores are occupied by HBA-X molecules, which are, based on the single crystal X-ray diffraction data, located in two positions with an occupancy of 0.5 each (Figure S17a, omitted for clarity in Figure 3e). The noncoordinating HBA-X molecules can be removed by solvent extraction followed by thermal activation. The coordination mode of the carboxylate groups of CAU-19-H are shown in Figure S17.[64]

The bond lengths found in **CAU-19-H** are in good agreement with the literature values. For Ce−O bonds, values between 2.374(8) and 2.730(6) Å were found, which are in good agreement with the literature values of 2.413(4) to 2.618(4) Å (CN: 8)[45] and 2.364(5) to 2.765(2) Å (CN: 12).[45,65] The C═C double bond length varies between 1.327(13) Å (arom. phenyl) and 1.512(11) Å (arom. pyrrole) and the N═C double bond length between 1.348(11) Å and 1.379(10) Å, which are also in good agreement with the literature values of 1.303(9) Å to 1.508(6) Å and 1.358(6) Å to 1.383(6) Å, respectively.[33,45]

Only one other porphyrine-based Ce-MOF of composition [Ce$_3$(H$_2$TCPP)$_2$(HCOO)(H$_2$O)$_3$] has been previously reported in the literature.[45] Its structure resembles some similarities to the one observed for **CAU-19**, but formate instead of benzoate ions are coordinated to the IBUs. In addition CeO$_{10}$ instead of CeO$_{12}$ polyhedra are incorporated in the trimeric IBUs which are interconnected by the linker molecules to form a framework similar to **CAU-19**.[45]

The structure of **Ce-PMOF-4NO$_2$**, [Ce$_2$(H$_2$TCPP)(BA-4NO$_2$)$_2$]·2DMF, consists of chains of trans corner-sharing CeO$_6$ polyhedra. The metal ions are bridged by the μ-oxygen atom of the carboxylate group of 4-nitrobenzoic acid (Figure 4). All other coordinating oxygen atoms stem from the carboxylate groups of the H$_2$TCPP^{4-} ions. The chains are connected by H$_2$TCPP^{4-} molecules to form a three-dimensional framework. Two types of pores are formed along [010], with pore diameters of 5.0 × 11.8 Å and 2.0 × 11.8 Å, respectively (Figure 4). This structure is similar to the ones of [M$_2$(μ-OH)$_2$(H$_2$TCPP)], M = Al, Ga, and In[36,37] where the bridging of the M^{3+} ions is accomplished through μ-OH groups. Since the BA-NO$_2^-$ ion is not located in a special position, the occupancy of the coligand was constrained to 0.25.

Thermal treatment of **CAU-18** between 250 and 300 °C leads to a microcrystalline product, of composition [Ce$_4$(H$_2$TCPP)$_3$], denoted **CAU-18a**, with low long-range order. At the activation temperature, removal of coordinating H$_2$O and DMF molecules takes place and a permanently porous compound is formed which adsorbs 22 H$_2$O molecules per formula unit. We anticipate condensation of the tetrameric units and formation of an open framework accessible for guest molecules. Thermogravimetric measurements confirm this hypothesis regarding the loss for DMF and H$_2$O molecules at 250 °C (Figure 8). IR spectroscopy confirms the absence of DMF molecules in **CAU-18a** (Figure 11).

Since Ce(III) and Ce(IV) compounds exhibit very distinct Ce L$_3$-edge XANES features, the corresponding measurements

DOI: 10.1021/acs.cgd.7b00450
Cryst. Growth Des. 2017, 17, 3462−3474

were performed for all title compounds to probe the oxidation state of Ce ions, similarly to our previous Ce MOFs studies.[21] As demonstrated by comparison with the spectra of CeO_2 and $Ce(NO_3)_3{\cdot}6H_2O$ reference compounds presented in Figure S18, all title compounds contain exclusively Ce^{3+} ions, which were formed during the synthesis from the Ce(IV) precursor $(NH_4)_2[Ce(NO_3)_6]$. It is worth to note that in the synthesis of Ce-UiO-66[21] the same reaction conditions were employed, but the tetravalent oxidation state was preserved during the reaction. Hence redox-active linker molecules such as H_6TCPP lead to the reduction of the Ce^{4+} ions during the reaction.

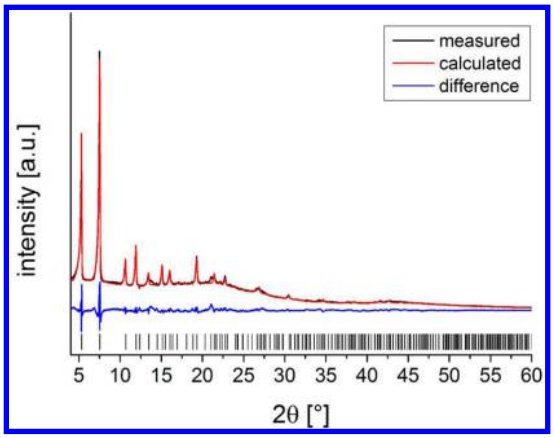

Figure 5. Result of the Rietveld-refinement of **Ce-PMOF-4NO$_2$**. Measured data are shown as a black line, calculated data as a red line, and the blue line gives the difference plot. Predicted peak positions are marked as vertical bars.

Sorption Properties. Sorption experiments were only carried out for **CAU-18a**, **CAU-19-X**, and **M-CAU-19-H** (M = Zn, Co) since **CAU-18** and **Ce-PMOF-4NO$_2$** transform to **CAU-18a** and **CAU-19-4NO$_2$** during the activation procedure. Prior to the sorption experiments all samples were activated at 170 °C under vacuum (10^{-2} kPa) for 16 h. Subsequently sorption experiments using N_2 at 77 K (Figures 6, S30 and S31) and H_2O at 298 K (Figure 7) as adsorptive were performed. The specific surface areas were determined using

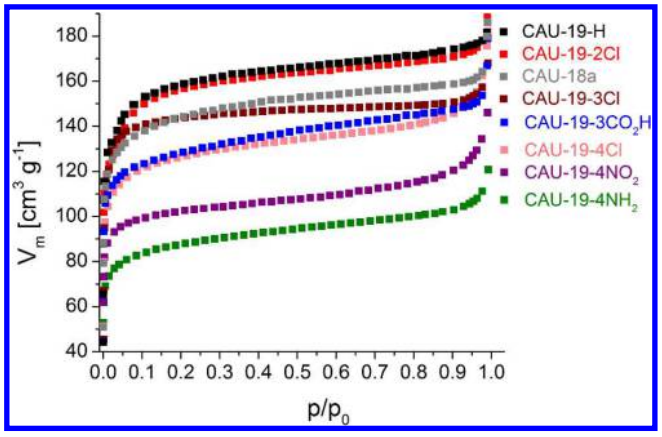

Figure 6. N_2-sorption isotherms of **CAU-18a** and **CAU-19-X** (X = H, 2Cl, 3Cl, 4Cl, $3CO_2H$, $4NH_2$, $4NO_2$) measured at 77 K. Only the adsorption branch is shown; desorption is omitted for clarity. All N_2-sorption isotherms including ad- and desorption are shown in the Supporting Information in Figure S30.

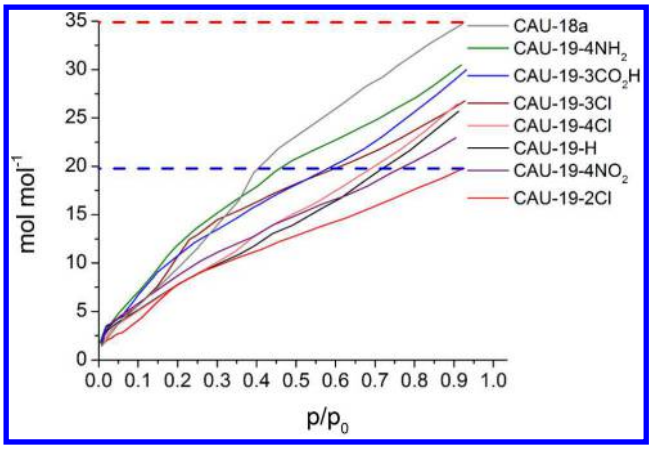

Figure 7. H_2O sorption isotherms of **CAU-18a** and **CAU-19-X** (X = H, 2Cl, 3Cl, 4Cl, $3CO_2H$, $4NH_2$, $4NO_2$) measured at 298 K (mol mol^{-1}). The red dashed line represents the sample with the highest uptake and the blue dashed line the sample with the lowest uptake, respectively.

the BET method and applying the method of Roquerol.[66,67] Micropore volumes V_m were determined by using the amount of adsorbed N_2 at the relative pressure $p/p_0 = 0.5$ (Table 3). All compounds are stable toward activation and sorption measurements as proven by PXRD measurements (Figure S32). All N_2 measurements lead to a type-1a isotherm as expected for microporous materials with pore diameters ≤1 nm.[67] **CAU-18a** has a specific surface area of a_{BET} = 550 m^2 g^{-1} and the **CAU-19-X** derivatives have a_{BET} values between 330 and 600 m^2 g^{-1} depending on the incorporated coligand. The metalated forms of **CAU-19-H** exhibit a specific surface area of 570 and 430 m^2 g^{-1} for Zn-**CAU-19-H** and Co-**CAU-19-H**, respectively. If the specific surface areas per millimol are taken into account, the value of Zn-**CAU-19-H** is identical with the one of the nonmetalated form, while for Co-**CAU-19-H** a slightly lower value is observed (Table 3).

A direct correlation of the steric demand of the different functional groups in **CAU-19-X** on the a_{BET} values is not observed. A coligand with a functional group in 2-position seems to lead to higher specific surface areas than ligands with groups in 3- or 4-position (Table 3). **CAU-19-4NH$_2$** has the smallest specific surface area of a_{BET} = 330 m^2 g^{-1} which is because not all HBA-NH_2 molecules could be removed from the pores during activation, as proven by NMR spectroscopy (Figure S10, one HBA-NH_2 molecule per formula unit remains in the pores). The rather low specific surface area of **CAU-19-4NO$_2$** of 400 m^2 g^{-1} is due to the low long-range order of the samples after the phase transformation.

The H_2O sorption measurements at 298 K of all samples show an uptake between 10.7 and 21.3 wt % and **CAU-18a** exhibits the highest uptake of 21.3 wt %, followed by **CAU-19-4NH$_2$** and **CAU-19-3CO$_2$H** with values of 16.6 and 16.0 wt %. This result is remarkable since in the N_2 sorption experiments these latter MOFs showed the lowest N_2 uptake, but it is probably due to strong H-bond interactions between the amino- and the carboxy-group of the incorporated benzoic acid derivatives in the pores with the adsorptive water.

Thermal and Chemical Stability. To investigate the thermal stability TG measurements of all samples and VT-PXRD studies for **CAU-18** and **CAU-19-H** were carried out.

The results of the TG measurements (Table S4, Figures 8 and 9 as well as Figures S33–S41) show two or three

DOI: 10.1021/acs.cgd.7b00450
Cryst. Growth Des. 2017, 17, 3462–3474

Table 3. Results of the Sorption Experiments (N_2 at 77 K and H_2O at 298.15 K) of CAU-18a, CAU-19-X (X = H, 2Cl, 3Cl, 4Cl, $3CO_2H$, $4NH_2$, $4NO_2$) and M-CAU-19-H (M = Zn, Co)[a]

	CAU-18a	H	Zn H	Co H	2Cl	3Cl	4Cl	$3CO_2H$	$4NH_2$	$4NO_2$
N_2 (a_{BET}) [m^2 g^{-1}]	550	600	570	430	590	580	480	490	330	400
[m^2 $mmol^{-1}$]	1620	1370	1374	1031	1390	1360	1130	1160	760	950
N_2 (V_m) [cm^3 g^{-1}]	0.24	0.26	0.24	0.19	0.25	0.23	0.21	0.21	0.15	0.17
H_2O (upt.) [mol mol^{-1}]	34.8	25.7			19.8	26.8	26.4	30.0	30.4	23.0
[wt %]	21.3	14.1			10.7	14.4	14.2	16.0	16.6	12.3

[a]The micropore volume was calculated at p/p_0 = 0.5.

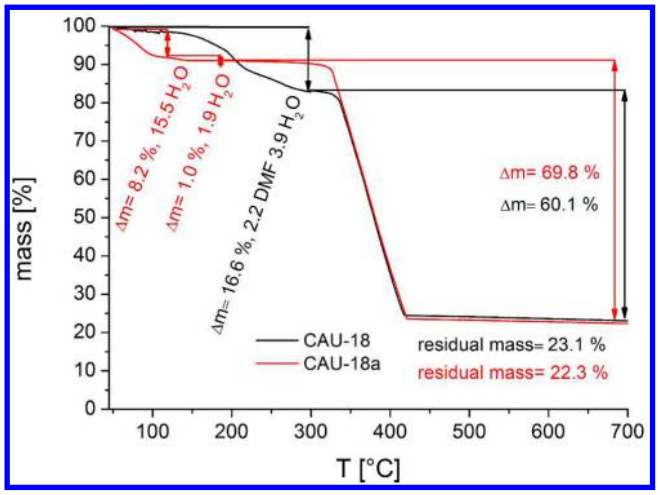

Figure 8. Thermogravimetric curve of **CAU-18** ($[Ce_4(H_2TCPP)_3(H_2O)_4(DMF)_2]$ and **CAU-18a** ($[Ce_4(H_2TCCP)_3]\cdot17.4H_2O$ (Table S4).

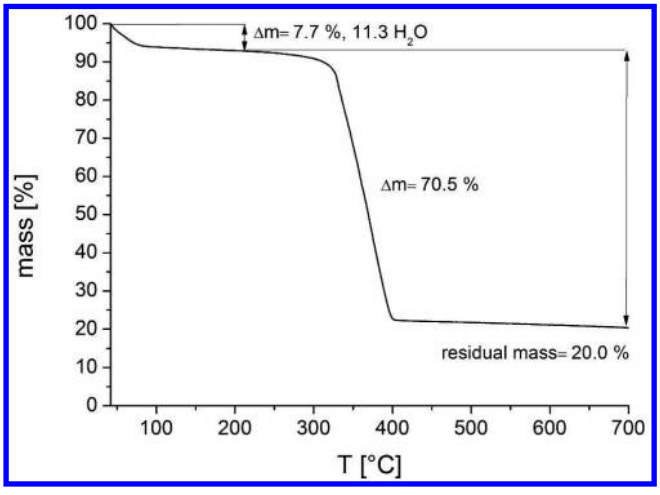

Figure 9. Thermogravimetric curve of **CAU-19-H**. Evaluation of the data reveals a molar ratio of metal/linker/benzoic acid/H_2O of 3.1:2:4:11.3 (Table S4).

characteristic steps of weight loss, respectively. The loss up to 100 °C is assigned to the evaporation of physisorbed water molecules. In the case of **CAU-18**, the removal of the coordinated DMF and water molecules occurs between 100 and 250 °C. The weight loss between 100 and 250 °C for **CAU-19-3CO$_2$H** is due to the evaporation of physisorbed DMF as confirmed by ^{1}H NMR spectroscopy (Figure S9). Above 330 °C the decomposition of the compounds take place, and CeO_2 is formed as the final product, as confirmed by PXRD measurements (Figure S42). In the TG curve of **CAU-18a** three steps of weight loss are observed. The first two steps up to 150 °C can be assigned to the loss of water molecules. No further weight loss up to 330 °C is observed, when the framework starts to decompose. These results demonstrate that the DMF molecules have been quantitatively removed during the transformation of **CAU-18** to **CAU-18a**, which was also confirmed by elemental analysis. In general, the results of the TG analysis fit well with the ones of the elemental analyses. Slight differences in the amounts of occluded solvent molecules are due to the storage of the samples prior to the measurements where guest molecules can be exchanged by atmospheric water molecules.

The results of the VT-PXRD studies of **CAU-18** and **CAU-19-H** are shown in Figure 10. These measurements show for **CAU-18** two phase transformations: one at 220 °C into an unknown intermediate and one at 300 °C into **CAU-18a**. Compared to the direct synthesis of **CAU-18a** (thermal treatment at 250 °C in air for 24 h) the phase transformation is delayed, probably because the VT-PXRD measurements are performed in the confinement of the quartz capillaries within 4 h instead of an open crucible within 24 h. The unknown intermediate was also sometimes observed in the direct synthesis at 250 °C but after shorter reaction times of 2 h. A first decrease of crystallinity is observed up to 380 °C, and the complete loss of crystallinity takes place at 490 °C. **CAU-19-H** shows a very similar behavior. Up to 380 °C, no remarkable loss of crystallinity is observable but a few reflections are shifted during the measurement. A decrease of crystallinity is observable at 385 °C, and the decomposition of the sample takes place at 480 °C. In comparison to the TG results, the measurements show higher decomposition temperatures (**CAU-18**: 450−500/330 °C, **CAU-19-H**: 450−550/330 °C), which is due to the confinement of the sample in a capillary during the VT-PXRD measurements.

To investigate the chemical stability, **CAU-18a** and **CAU-19-H** were exemplarily treated in different solvents (2 M HCl, 2 M NaOH, 100% acetic acid, H_2O, MeOH, EtOH, acetone, dichloromethane) at RT for 24 h under stirring. After the treatment, the samples were isolated by filtration and measured by PXRD. The results of the chemical stability tests (Figure S43) reveal that both MOFs are stable in all tested organic solvents and water, but show a complete decomposition in 2 M HCl and 2 M NaOH and decrease of crystallinity in 100% acetic acid.

In Situ X-ray Diffraction. To learn more about the formation of **CAU-18** and **CAU-19-H** in situ crystallization studies were carried out employing synchrotron radiation.[68] These MOFs are ideal candidates for such studies since they are formed within short reaction times of 1−2 h. In addition to the detection of possible crystalline intermediates X-ray diffraction (XRD) crystallization studies are a suitable method to determine kinetic parameters such as rate constants for nucleation (k_n) and crystal growth (k_g) as well as the respective

DOI: 10.1021/acs.cgd.7b00450
Cryst. Growth Des. 2017, 17, 3462−3474

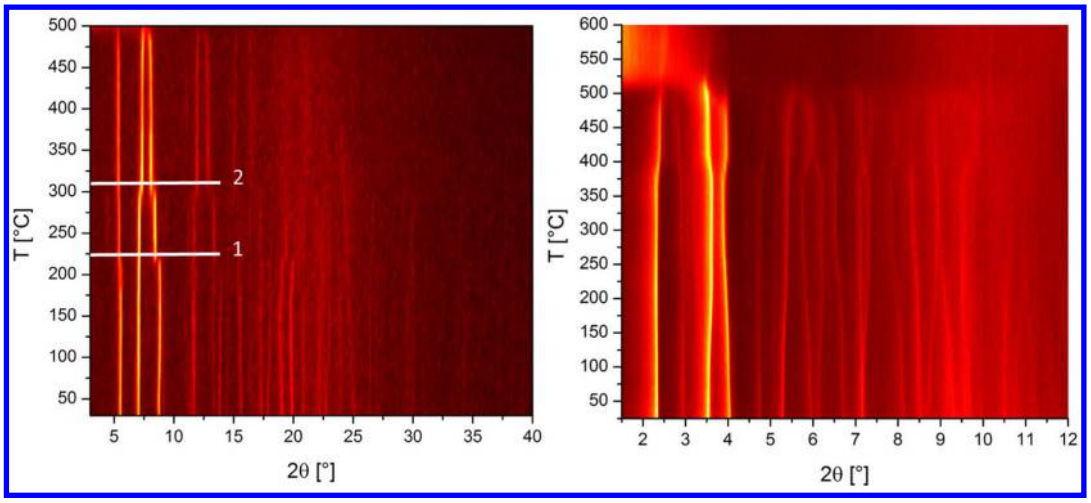

Figure 10. Results of the VT-PXRD studies of **CAU-18** (left, Cu Kα_1 radiation) and **CAU-19-H** (right, Mo Kα_1 radiation) measured in open quartz capillaries (0.5 mm) under atmospheric conditions. The label 1 indicates the phase transformation into an unknown intermediate and the label 2 the phase transformation into **CAU-18a**.

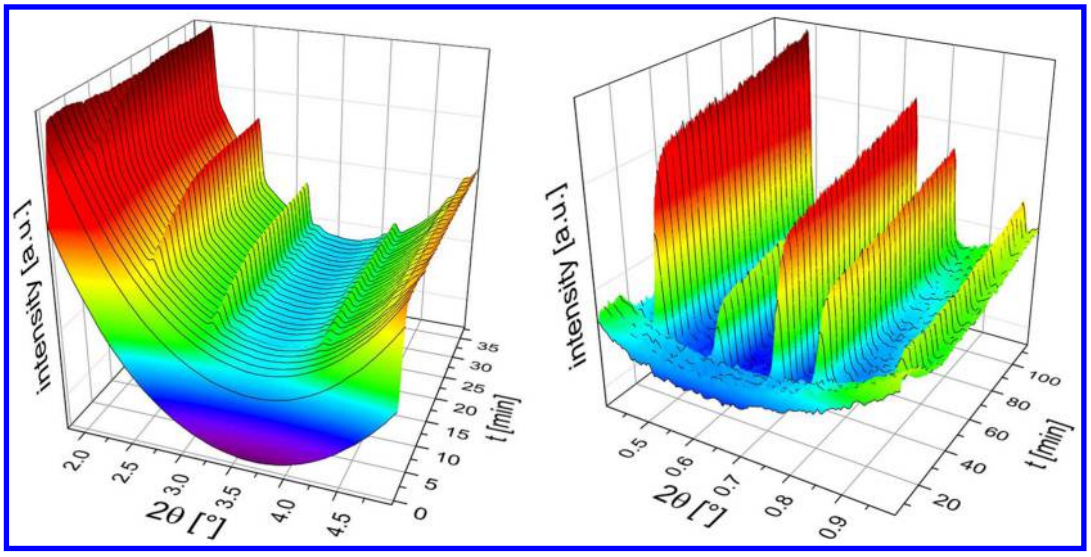

Figure 11. Results of the in situ XRD crystallization of **CAU-18** (left) and **CAU-19-H** (right) at a reaction temperature of 120 °C. Measurements were carried out at beamlines P09 and P07B, PETRA III, DESY, Hamburg.

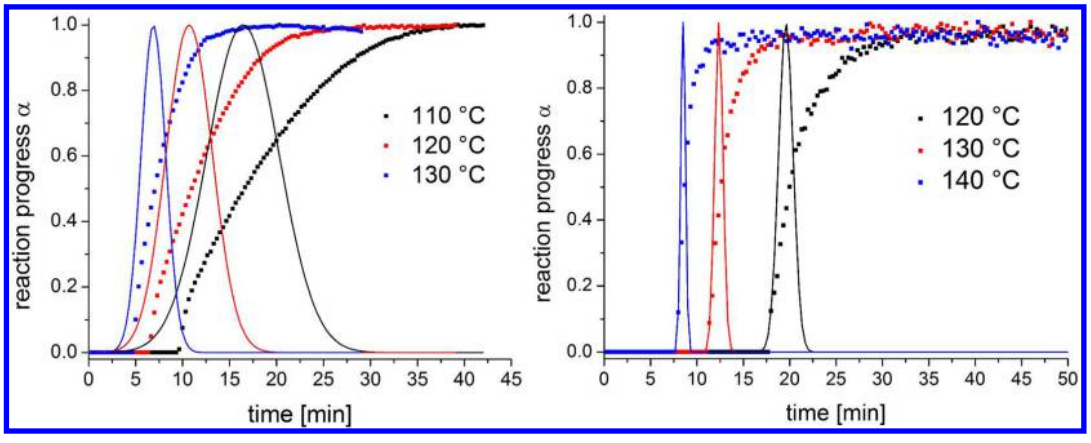

Figure 12. Reaction progress α (filled squares) and probability of nucleation P_n (line) of **CAU-18** (left) and **CAU-19-H** (right) as determined at the different reaction temperatures.

Arrhenius activation energies (E_A) and the probability of nucleation (P_n) and have been reported for several MOFs like MIL-53,[8] MOF-14,[10] MIL-100,[9] and CAU-13.[69] Crystallization studies have also been reported for other compounds which are

DOI: 10.1021/acs.cgd.7b00450
Cryst. Growth Des. 2017, 17, 3462−3474

Table 4. Rate Constants for Nucleation (k_n) and Crystal Growth (k_g), Nucleation Parameter b, Induction Time (t_{ind}), Time to Reach Reaction Completeness (t_{com}) and Maximum of Probability of Nucleation (P_n) as Obtained Using the Method of Gualtieri[12a]

	$a = k_n^{-1}$	k_g	b	t_{ind} [min]	t_{com} [min]	P_n (max) [min]
CAU-18 110 °C	16.43	0.09	5.43	9.7	37.0	16.3
CAU-18 120 °C	10.70	0.13	3.50	6.7	28.3	10.7
CAU-18 130 °C	6.89	0.19	1.86	5.0	17.7	7.0
CAU-19-H 120 °C	19.58	0.08	1.11	16.0 (13.0)	34.3 (31.3)	19.7
CAU-19-H 130 °C	12.36	0.13	0.63	9.7 (6.7)	22.3 (19.3)	12.3
CAU-19-H 140 °C	8.50	0.19	0.35	6.3 (3.3)	17.7 (14.7)	8.5

[a]Values in brackets represent the reduced values t_{ind} and t_{com} for injection of the metal salt solution after 3 min to initiate the formation of CAU-19-H.

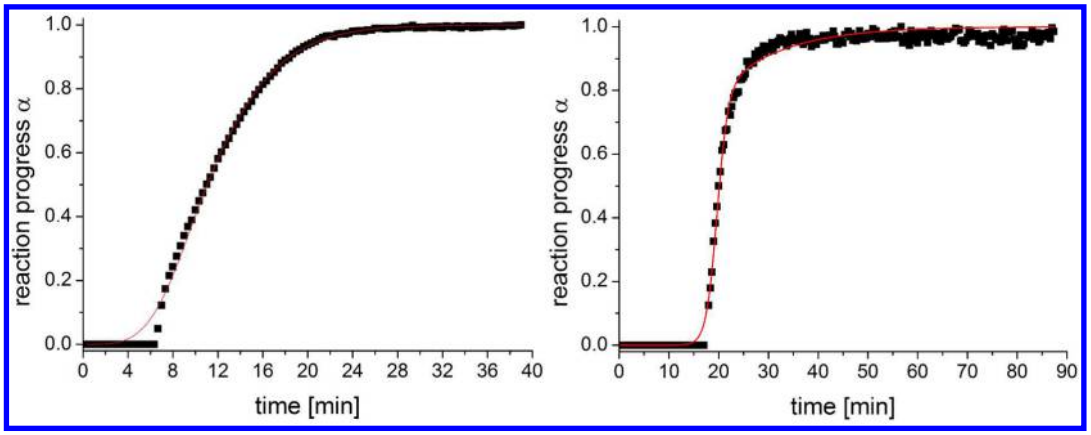

Figure 13. Gualtieri-fit of the reaction progress for the reactions carried out at 120 °C. Left, formation of **CAU-18** and right, formation of **CAU-19-H**. The results of the fits are summarized in Figures S50 and S52.

obtained under solvothermal reaction conditions like zeolites,[12] polyoxovanadates,[70] and thioantimonates.[71]

The crystallization of **CAU-18** was carried out at three different reaction temperatures (110, 120, and 130 °C). The linker (H_6TCPP, 20 mg, 2.53 × 10^{-2} mmol), 2400 μL of *N*,*N*-dimethylformamide (DMF), 350 μL of dist. H_2O and 94.5 μL of a 0.53 mol/L solution of $(NH_4)_2[Ce(NO_3)_6]$ in dist. H_2O were placed in a borosilicate glass vessel (V_{max} = 5 mL). After homogenization by shaking, the glass vessel was immediately placed inside the reactor. The reaction mixture was heated to the target temperature within 3 min and stirred during the reaction while collecting powder diffraction data.

The ex situ crystallization study of **CAU-19-H** indicated a very fast formation. Hence the reactor was modified to include a syringe pump system which was employed to start the reaction remotely from the control hutch. The synthesis was carried out at three different reaction temperatures (120, 130, and 140 °C). A solution of H_6TCPP (20 mg, 2.53 × 10^{-2} mmol) and benzoic acid (550 mg, 4.5 mmol) in 2400 μL of DMF and 200 μL of H_2O was placed in a borosilicate glass vessel (V_{max} = 5 mL) and heated to the target temperature (ca. 3 min) under stirring while continuously measuring XRD data. Subsequently 226 μL of a 0.5333 mol/L solution of $(NH_4)_2[Ce(NO_3)_6]$ in dist. H_2O was added via injection to initiate the reaction.

The results of the in situ crystallization of **CAU-18** and **CAU-19-H** are shown for the reactions at 120 °C in Figure 11; further in situ crystallization plots are shown in Figures S44–S48. In order to investigate the kinetics of crystallization, the normalized peak areas at the different reaction times, which correspond to the reaction progress α, were determined. For **CAU-18** the [020] and for **CAU-19-H** the [100] reflections were used, which are the ones with the highest intensity. The reaction progress α at different reaction temperatures is shown in Figure 12. As expected, the induction time (t_{ind}), in which no crystalline products are observed, and the total reaction time to achieve full conversion (t_{com}) are shorter at higher temperatures (Figure 12 and Table 4).

The method of Gualtieri was employed to determine the kinetic constants of the crystallization process of **CAU-18** and **CAU-19-H**.[12] In this model the nucleation and the crystal growth are taken into account and are considered as separate processes (eq 1).

$$\alpha = \frac{1}{1 + \exp\left[-\left(\frac{t-a}{b}\right)\right]}\{1 - \exp(k_g t)^n]\} \quad (1)$$

The reaction progress α is a nonlinear function depending on the reaction time t and the parameters $a = k_n^{-1}$ (reciprocal rate constant of nucleation), b (a constant related to nucleation), k_g (rate constant of crystal growth), and n, which represents the dimensionality of the crystal growth.[12] To find the right value for n, all dimensionalities were tested, and the best fit, n = 3 for **CAU-18** and n = 1 for **CAU-19-H** was found, which was substantiated by the SEM measurements (Figures S13–S14). The results of the Gualtieri fits for the reaction at 120 °C for both compounds are shown in Figure 13, and the resulting parameters are listed in Table 4. The Gualtieri fits for the data obtained at the other reaction temperatures are shown in Figures S49–S54. The rate constants for nucleation and crystal growth increase with temperature and can be used to calculate the probability of nucleation P_n which is given in eq 2.

DOI: 10.1021/acs.cgd.7b00450
Cryst. Growth Des. 2017, 17, 3462–3474

$$P_n = e^{-(t-a)^2/b^2} \quad (2)$$

P_n is plotted versus time and depends on the Gualtieri constants a and b. The maximum of the probability of nucleation is shifted to smaller reaction times with increasing temperature (Figure 12 and Table 4). The Arrhenius activation energy for nucleation and crystal growth can be obtained by plotting $\ln(k)$ vs $1/T$ (Figures S55–S58). The Arrhenius activation energies were determined as 56(1) and 56(3) kJ mol^{-1} for nucleation and 48(1) and 58(5) kJ mol^{-1} for crystal growth for **CAU-18** and **CAU-19-H**, respectively. The activation energies are in the same order of magnitude and in good agreement with other previous reported MOFs (Mn-MIL-100: 89.9/126.5 kJ mol^{-1} (ref 9), MOF-14: 64–83 kJ mol^{-1} (ref 10), CAU-13: 76–77 kJ mol^{-1} (ref 69), and CAU-1: 131–136 kJ mol^{-1} (ref 11)).

CONCLUSION

We demonstrated the successful synthesis and characterization of four new porphyrin-based Ce-MOFs, **CAU-18**, $[Ce_4(H_2TCPP)_3(DMF)_2(H_2O)_4]$, **CAU-18a**, $[Ce_4(H_2TCPP)_3]\cdot 22\ H_2O$, **CAU-19-X**, $Ce_3(H_2TCPP)_2(BA\text{-}X)(HBA\text{-}X/H_2O)_2]\cdot 2\ HBA\cdot xH_2O$ (X = H, 2Cl, 3Cl, 4Cl, $3CO_2H$, $4NH_2$, $4NO_2$), and **Ce-PMOF-4NO$_2$**, $[Ce_2(H_2TCPP)(C_7H_4O_2NO_2)_2]\cdot 2DMF$ (H_6TCPP = 4-tetracarboxyphenylporphyrin).

Considering this observed structural diversity induced by the presence/nature of the coligand employed, it could be very interesting to evaluate the other lanthanide ions in a similar manner. Furthermore, the metalated form of **CAU-19-H**, **M-CAU-19-H** with M = Zn and Co were obtained. Despite the use of $(NH_4)_2[Ce(NO_3)_6]$ as a source of Ce in all syntheses, all compounds contain exclusively Ce^{3+} ions. The trivalent oxidation state was unequivocally confirmed by XANES measurements. Thermal treatment of **CAU-18** at 250 °C leads to the removal of DMF molecules and the permanently porous compound **CAU-18a** formed. Phase transformation of Ce-PMOF-NO_2 to **CAU-19**-NO_2 is observed in organic solvents at 70 °C within 72 h. **CAU-18a** and all **CAU-19-X** derivatives are permanently porous with specific surface areas of 330–600 m^2 g^{-1} as determined from N_2 physisorption measurements at 77 K, and they are also porous toward H_2O with an uptake between 10.7 and 21.3 wt %. The in situ crystallization studies revealed the expected temperature dependent increase of the rate constants for the formation of **CAU-18** and **CAU-19-H**.

In this context it could be very interesting to further investigate the formation of the title compounds by in situ XAS or EXAFS studies to gain insight into the reduction of the metal source and the relevance for the formation of Ce^{3+}/Ce^{4+} MOFs.

ASSOCIATED CONTENT

Supporting Information

The Supporting Information is available free of charge on the ACS Publications website at DOI: 10.1021/acs.cgd.7b00450.

Details of the synthesis and characterization of H_6TCPP, Co–H_4TCPP and information on the characterization of all obtained compounds, including ^1H NMR spectroscopy, Pawley fits, XANES spectra, structural representations, thermogravimetric measurements and IR-spectroscopy (PDF)

Accession Codes

CCDC 1539771–1539772 contain the supplementary crystallographic data for this paper. These data can be obtained free of charge via www.ccdc.cam.ac.uk/data_request/cif, or by emailing data_request@ccdc.cam.ac.uk, or by contacting The Cambridge Crystallographic Data Centre, 12 Union Road, Cambridge CB2 1EZ, UK; fax: +44 1223 336033.

AUTHOR INFORMATION

Corresponding Author

*E-mail: stock@ac.uni-kiel.de.

ORCID

Helge Reinsch: 0000-0001-5288-1135

Norbert Stock: 0000-0002-0339-7352

Notes

The authors declare no competing financial interest.

ACKNOWLEDGMENTS

We appreciate support from the Deutsche Forschungsgemeinschaft (SPP-1415; STO 643/6-2). We would like to acknowledge Milan Köppen for the development of software tools used for data treatment and DESY for the allocation of beamtime. Furthermore, we thank Jörg Strempfer and the beamline staff of beamline P07 and P09 for their support during the beamtime as well as HZG and Norbert Schell. This work has been supported by the MATsynCELL project through the Röntgen-Ångström Cluster, supported by the Swedish Research Council and the German Federal Ministry of Education and Research (BMBF). A.V.S. acknowledges the Mega-grant of the Russian Federation Government No. 14.Y26.31.0001. K.A.L. acknowledges the support from the Russian Foundation for Basic Research, Project No. 16-32-00572 mol_a. Furthermore, we thank Simon Smolders from the KU Leuven for measuring the TG curves of Zn- and Co-CAU-19-H, Figures S40 and S41.

REFERENCES

(1) Furukawa, H.; Cordova, K. E.; O'Keeffe, M.; Yaghi, O. M. The Chemistry and Applications of Metal-Organic Frameworks. *Science* **2013**, *341*.123044410.1126/science.1230444

(2) Stock, N.; Reinsch, H.; Schilling, L.-H. CHAPTER 2 Synthesis of MOFs. *Metal Organic Frameworks as Heterogeneous Catalysts*; The Royal Society of Chemistry, 2013; pp 9–30.

(3) Zhou, H.-C.; Long, J. R.; Yaghi, O. M. Introduction to Metal–Organic Frameworks. *Chem. Rev.* **2012**, *112*, 673–674.

(4) Yaghi, O. M.; O'Keeffe, M.; Ockwig, N. W.; Chae, H. K.; Eddaoudi, M.; Kim, J. Reticular synthesis and the design of new materials. *Nature* **2003**, *423*, 705–714.

(5) Sun, C.-Y.; Qin, C.; Wang, X.-L.; Su, Z.-M. Metal-organic frameworks as potential drug delivery systems. *Expert Opin. Drug Delivery* **2013**, *10*, 89–101.

(6) Janiak, C.; Vieth, J. K. MOFs, MILs and more: concepts, properties and applications for porous coordination networks (PCNs). *New J. Chem.* **2010**, *34*, 2366–2388.

(7) Mueller, U.; Schubert, M.; Teich, F.; Puetter, H.; Schierle-Arndt, K.; Pastre, J. Metal-organic frameworks-prospective industrial applications. *J. Mater. Chem.* **2006**, *16*, 626–636.

(8) Millange, F.; Medina, M. I.; Guillou, N.; Férey, G.; Golden, K. M.; Walton, R. I. Time-Resolved In Situ Diffraction Study of the Solvothermal Crystallization of Some Prototypical Metal–Organic Frameworks. *Angew. Chem., Int. Ed.* **2010**, *49*, 763–766.

(9) Reinsch, H.; Stock, N. Formation and characterisation of Mn-MIL-100. *CrystEngComm* **2013**, *15*, 544–550.

(10) Millange, F.; El Osta, R.; Medina, M. E.; Walton, R. I. A time-resolved diffraction study of a window of stability in the synthesis of a

DOI: 10.1021/acs.cgd.7b00450
Cryst. Growth Des. 2017, 17, 3462–3474

copper carboxylate metal-organic framework. *CrystEngComm* **2011**, *13*, 103−108.
(11) Ahnfeldt, T.; Moellmer, J.; Guillerm, V.; Staudt, R.; Serre, C.; Stock, N. High-Throughput and Time-Resolved Energy-Dispersive X-Ray Diffraction (EDXRD) Study of the Formation of CAU-1-(OH)2: Microwave and Conventional Heating. *Chem. - Eur. J.* **2011**, *17*, 6462−6468.
(12) Gualtieri, F. A. Synthesis of sodium zeolites from a natural halloysite. *Phys. Chem. Miner.* **2001**, *28*, 719−728.
(13) Feng, D.; Jiang, H.-L.; Chen, Y.-P.; Gu, Z.-Y.; Wei, Z.; Zhou, H.-C. Metal−Organic Frameworks Based on Previously Unknown Zr8/Hf8 Cubic Clusters. *Inorg. Chem.* **2013**, *52*, 12661−12667.
(14) Feng, D.; Chung, W.-C.; Wei, Z.; Gu, Z.-Y.; Jiang, H.-L.; Chen, Y.-P.; Darensbourg, D. J.; Zhou, H.-C. Construction of Ultrastable Porphyrin Zr Metal−Organic Frameworks through Linker Elimination. *J. Am. Chem. Soc.* **2013**, *135*, 17105−17110.
(15) Gallagher, A. T.; Kelty, M. L.; Park, J. G.; Anderson, J. S.; Mason, J. A.; Walsh, J. P. S.; Collins, S. L.; Harris, T. D. Dioxygen binding at a four-coordinate cobaltous porphyrin site in a metal-organic framework: structural, EPR, and O2 adsorption analysis. *Inorg. Chem. Front.* **2016**, *3*, 536−540.
(16) Hod, I.; Sampson, M. D.; Deria, P.; Kubiak, C. P.; Farha, O. K.; Hupp, J. T. Fe-Porphyrin-Based Metal−Organic Framework Films as High-Surface Concentration, Heterogeneous Catalysts for Electrochemical Reduction of CO2. *ACS Catal.* **2015**, *5*, 6302−6309.
(17) Chang, T.-H.; Kung, C.-W.; Chen, H.-W.; Huang, T.-Y.; Kao, S.-Y.; Lu, H.-C.; Lee, M.-H.; Boopathi, K. M.; Chu, C.-W.; Ho, K.-C. Planar Heterojunction Perovskite Solar Cells Incorporating Metal−Organic Framework Nanocrystals. *Adv. Mater. (Weinheim, Ger.)* **2015**, *27*, 7229−7235.
(18) Kung, C.-W.; Chang, T.-H.; Chou, L.-Y.; Hupp, J. T.; Farha, O. K.; Ho, K.-C. Post metalation of solvothermally grown electroactive porphyrin metal-organic framework thin films. *Chem. Commun.* **2015**, *51*, 2414−2417.
(19) Liu, Y.; Howarth, A. J.; Hupp, J. T.; Farha, O. K. Selective Photooxidation of a Mustard-Gas Simulant Catalyzed by a Porphyrinic Metal−Organic Framework. *Angew. Chem., Int. Ed.* **2015**, *54*, 9001−9005.
(20) Guo, Z.; Chen, B. Recent developments in metal-metalloporphyrin frameworks. *Dalton Trans* **2015**, *44*, 14574−14583.
(21) Lammert, M.; Wharmby, M. T.; Smolders, S.; Bueken, B.; Lieb, A.; Lomachenko, K. A.; Vos, D. D.; Stock, N. Cerium-based metal organic frameworks with UiO-66 architecture: synthesis, properties and redox catalytic activity. *Chem. Commun.* **2015**, *51*, 12578−12581.
(22) Alves, E.; Faustino, M. A. F.; Neves, M. G. P. M. S.; Cunha, Â.; Nadais, H.; Almeida, A. Potential applications of porphyrins in photodynamic inactivation beyond the medical scope. *J. Photochem. Photobiol., C* **2015**, *22*, 34−57.
(23) Huang, H.; Song, W.; Rieffel, J.; Lovell, J. F. Emerging Applications of Porphryins in Photomedicine. *Front. Phys.* **2015**, *3*.10.3389/fphy.2015.00023
(24) Lu, K.; He, C.; Lin, W. A Chlorin-Based Nanoscale Metal−Organic Framework for Photodynamic Therapy of Colon Cancers. *J. Am. Chem. Soc.* **2015**, *137*, 7600−7603.
(25) Devic, T.; Serre, C. High valence 3p and transition metal based MOFs. *Chem. Soc. Rev.* **2014**, *43*, 6097−6115.
(26) Gao, W.-Y.; Chrzanowski, M.; Ma, S. Metal-metalloporphyrin frameworks: a resurging class of functional materials. *Chem. Soc. Rev.* **2014**, *43*, 5841−5866.
(27) Guo, Z.; Chen, B. Recent developments in metal-metalloporphyrin frameworks. *Dalton Trans* **2015**, *44*, 14574−14583.
(28) Huh, S.; Kim, S.-J.; Kim, Y. Porphyrinic metal-organic frameworks from custom-designed porphyrins. *CrystEngComm* **2016**, *18*, 345.
(29) Kosal, M. E.; Chou, J.-H.; Wilson, S. R.; Suslick, K. S. A functional zeolite analogue assembled from metalloporphyrins. *Nat. Mater.* **2002**, *1*, 118−121.
(30) Goldberg, I. Metalloporphyrin Molecular Sieves. *Chem. - Eur. J.* **2000**, *6*, 3863−3870.
(31) Feng, D.; Gu, Z.-Y.; Chen, Y.-P.; Park, J.; Wei, Z.; Sun, Y.; Bosch, M.; Yuan, S.; Zhou, H.-C. A Highly Stable Porphyrinic Zirconium Metal−Organic Framework with shp-a Topology. *J. Am. Chem. Soc.* **2014**, *136*, 17714−17717.
(32) Jiang, H.-L.; Feng, D.; Wang, K.; Gu, Z.-Y.; Wei, Z.; Chen, Y.-P.; Zhou, H.-C. An Exceptionally Stable, Porphyrinic Zr Metal−Organic Framework Exhibiting pH-Dependent Fluorescence. *J. Am. Chem. Soc.* **2013**, *135*, 13934−13938.
(33) Morris, W.; Volosskiy, B.; Demir, S.; Gándara, F.; McGrier, P. L.; Furukawa, H.; Cascio, D.; Stoddart, J. F.; Yaghi, O. M. Synthesis, Structure, and Metalation of Two New Highly Porous Zirconium Metal−Organic Frameworks. *Inorg. Chem.* **2012**, *51*, 6443−6445.
(34) Bai, Y.; Dou, Y.; Xie, L.-H.; Rutledge, W.; Li, J.-R.; Zhou, H.-C. Zr-based metal-organic frameworks: design, synthesis, structure, and applications. *Chem. Soc. Rev.* **2016**, *45*, 2327−2367.
(35) Feng, D.; Jiang, H.-L.; Chen, Y.-P.; Gu, Z.-Y.; Wei, Z.; Zhou, H.-C. Metal−Organic Frameworks Based on Previously Unknown Zr8/Hf8 Cubic Clusters. *Inorg. Chem.* **2013**, *52*, 12661−12667.
(36) Fateeva, A.; Chater, P. A.; Ireland, C. P.; Tahir, A. A.; Khimyak, Y. Z.; Wiper, P. V.; Darwent, J. R.; Rosseinsky, M. J. A Water-Stable Porphyrin-Based Metal−Organic Framework Active for Visible-Light Photocatalysis. *Angew. Chem.* **2012**, *124*, 7558−7562.
(37) Rhauderwiek, T.; Waitschat, S.; Wuttke, S.; Reinsch, H.; Bein, T.; Stock, N. Nanoscale Synthesis of Two Porphyrin-Based MOFs with Gallium and Indium. *Inorg. Chem.* **2016**, *55*, 5312−5319.
(38) Gao, W.-Y.; Zhang, Z.; Cash, L.; Wojtas, L.; Chen, Y.-S.; Ma, S. Two rare indium-based porous metal-metalloporphyrin frameworks exhibiting interesting CO2 uptake. *CrystEngComm* **2013**, *15*, 9320−9323.
(39) Johnson, J. A.; Luo, J.; Zhang, X.; Chen, Y.-S.; Morton, M. D.; Echeverría, E.; Torres, F. E.; Zhang, J. Porphyrin-Metalation-Mediated Tuning of Photoredox Catalytic Properties in Metal−Organic Frameworks. *ACS Catal.* **2015**, *5*, 5283−5291.
(40) Johnson, J. A.; Zhang, X.; Reeson, T. C.; Chen, Y.-S.; Zhang, J. Facile Control of the Charge Density and Photocatalytic Activity of an Anionic Indium Porphyrin Framework via in Situ Metalation. *J. Am. Chem. Soc.* **2014**, *136*, 15881−15884.
(41) Fateeva, A.; Devautour-Vinot, S.; Heymans, N.; Devic, T.; Grenèche, J.-M.; Wuttke, S.; Miller, S.; Lago, A.; Serre, C.; de Weireld, G.; et al. Series of Porous 3-D Coordination Polymers Based on Iron(III) and Porphyrin Derivatives. *Chem. Mater.* **2011**, *23*, 4641−4651.
(42) Fateeva, A.; Clarisse, J.; Pilet, G.; Grenèche, J.-M.; Nouar, F.; Abeykoon, B. K.; Guegan, F.; Goutaudier, C.; Luneau, D.; Warren, J. E.; et al. Iron and Porphyrin Metal−Organic Frameworks: Insight into Structural Diversity, Stability, and Porosity. *Cryst. Growth Des.* **2015**, *15*, 1819−1826.
(43) Wang, K.; Feng, D.; Liu, T.-F.; Su, J.; Yuan, S.; Chen, Y.-P.; Bosch, M.; Zou, X.; Zhou, H.-C. A Series of Highly Stable Mesoporous Metalloporphyrin Fe-MOFs. *J. Am. Chem. Soc.* **2014**, *136*, 13983−13986.
(44) Yang, F.; Jing, L.; Ji, L.; Liu, Q.; Zhang, X. Design, fabrication and the relative catalytic properties of metal-organic framework complexes based on tetra(4-carboxyphenyl)porphyrin and cerium ions. *CrystEngComm* **2014**, *16*, 4274−4280.
(45) Lipstman, S.; Goldberg, I. 2D and 3D coordination networks of tetra(carboxyphenyl)-porphyrins with cerium and thulium ions. *J. Mol. Struct.* **2008**, *890*, 101−106.
(46) Muniappan, S.; Lipstman, S.; George, S.; Goldberg, I. Porphyrin Framework Solids. Synthesis and Structure of Hybrid Coordination Polymers of Tetra(carboxyphenyl)porphyrins and Lanthanide-Bridging Ions. *Inorg. Chem.* **2007**, *46*, 5544−5554.
(47) Lipstman, S.; Muniappan, S.; George, S.; Goldberg, I. Framework coordination polymers of tetra(4-carboxyphenyl)-porphyrin and lanthanide ions in crystalline solids. *Dalton Trans* **2007**, 3273−3281.
(48) Jeong, E.-Y.; Ansari, M. B.; Mo, Y.-H.; Park, S.-E. Removal of Cu(II) from water by tetrakis(4-carboxyphenyl) porphyrin-functionalized mesoporous silica. *J. Hazard. Mater.* **2011**, *185*, 1311−1317.

DOI: 10.1021/acs.cgd.7b00450
Cryst. Growth Des. 2017, 17, 3462−3474

(49) Harada, A.; Yamaguchi, H.; Okamoto, K.; Fukushima, H.; Shiotsuki, K.; Kamachi, M. Control of Photoinduced Electron Transfer from Zinc-Porphyrin to Methyl Viologen by Supramolecular Formation between Monoclonal Antibody and Zinc-Porphyrin. *Photochem. Photobiol.* **1999**, *70*, 298−302.
(50) Garcia, G.; Sol, V.; Lamarche, F.; Granet, R.; Guilloton, M.; Champavier, Y.; Krausz, P. Synthesis and photocytotoxic activity of new chlorin−polyamine conjugates. *Bioorg. Med. Chem. Lett.* **2006**, *16*, 3188−3192.
(51) Chen, W.; Fukuzumi, S. Change in Supramolecular Networks through In Situ Esterification of Porphyrins. *Eur. J. Inorg. Chem.* **2009**, *2009*, 5494−5505.
(52) Feng, D.; Gu, Z.-Y.; Li, J.-R.; Jiang, H.-L.; Wei, Z.; Zhou, H.-C. Zirconium-Metalloporphyrin PCN-222: Mesoporous Metal−Organic Frameworks with Ultrahigh Stability as Biomimetic Catalysts. *Angew. Chem.* **2012**, *124*, 10453−10456.
(53) *SAINT V9.32B*, Bruker AXS Inc.: Madison, Wisconsin, USA, 2012.
(54) Sheldrick, G. A short history of SHELX. *Acta Crystallogr., Sect. A: Found. Crystallogr.* **2008**, *64*, 112−122.
(55) Dolomanov, O. V.; Bourhis, L. J.; Gildea, R. J.; Howard, J. A. K.; Puschmann, H. OLEX2: a complete structure solution, refinement and analysis program. *J. Appl. Crystallogr.* **2009**, *42*, 339−341.
(56) Klementiev, K.; Chernikov, R. XAFSmass: a program for calculating the optimal mass of XAFS samples. *J. Phys.: Conf. Ser.* **2016**, *712*, 12008.
(57) Coelho, A. *TOPAS-Academic V4.1*; Coelho Software, 2007.
(58) Brandenburg, K. *Diamond Version 3*; Crystal Impact GbR: Bonn, 2012.
(59) Strempfer, J.; Francoual, S.; Reuther, D.; Shukla, D. K.; Skaugen, A.; Schulte-Schrepping, H.; Kracht, T.; Franz, H. Resonant scattering and diffraction beamline P09 at PETRA III. *J. Synchrotron Radiat.* **2013**, *20*, 541−549.
(60) Brokmeier, H. G.; Müller, M.; Pranzas, P. K.; Schreyer, A.; Staron, P. The High Energy Materials Science Beamline (HEMS) at PETRA III. *Mater. Sci. Forum* **2014**, *772*, 57−61.
(61) Heidenreich, N.; Rütt, U.; Köppen, M.; Inge, A. K.; Beier, S.; Dippel, A.-C.; Suren, R.; Stock, N. A multi-purpose reaction cell for the investigation of reactions under solvothermal conditions. *Rev. Sci. Instrum.* **2017**, submitted.
(62) Afzal, S.; Daoud, W. A.; Langford, S. J. Self-cleaning cotton by porphyrin-sensitized visible-light photocatalysis. *J. Mater. Chem.* **2012**, *22*, 4083−4088.
(63) Rochford, J.; Chu, D.; Hagfeldt, A.; Galoppini, E. Tetrachelate Porphyrin Chromophores for Metal Oxide Semiconductor Sensitization: Effect of the Spacer Length and Anchoring Group Position. *J. Am. Chem. Soc.* **2007**, *129*, 4655−4665.
(64) Coxall, R. A.; Harris, S. G.; Henderson, D. K.; Parsons, S.; Tasker, P. A.; Winpenny, R. E. P. Inter-ligand reactions: in situ formation of new polydentate ligands. *J. Chem. Soc., Dalton Trans.* **2000**, 2349−2356.
(65) Han, Y.; Li, X.; Li, L.; Ma, C.; Shen, Z.; Song, Y.; You, X. Structures and Properties of Porous Coordination Polymers Based on Lanthanide Carboxylate Building Units. *Inorg. Chem.* **2010**, *49*, 10781−10787.
(66) Rouquerol, J.; Avnir, D.; Fairbridge, C. W.; Everett, D. H.; Haynes, J. M.; Pernicone, N.; Ramsay, J. D. F.; Sing, K. S. W.; Unger, K. K. Recommendations for the characterization of porous solids (Technical Report). *Pure Appl. Chem.* **1994**, *66*, 1739−1758.
(67) Thommes, M.; Kaneko, K.; Neimark, A. V.; Olivier, J. P.; Rodriguez-Reinoso, F.; Rouquerol, J.; Sing, K. S. W. Physisorption of gases, with special reference to the evaluation of surface area and pore size distribution (IUPAC Technical Report). *Pure Appl. Chem.* **2015**, *87*.10.1515/pac-2014-1117
(68) Pienack, N.; Bensch, W. In-Situ Monitoring of the Formation of Crystalline Solids. *Angew. Chem., Int. Ed.* **2011**, *50*, 2014−2034.
(69) Niekiel, F.; Ackermann, M.; Guerrier, P.; Rothkirch, A.; Stock, N. Aluminum-1,4-cyclohexanedicarboxylates: High-Throughput and Temperature-Dependent in Situ EDXRD Studies. *Inorg. Chem.* **2013**, *52*, 8699−8705.
(70) Antonova, E.; Seidlhofer, B.; Wang, J.; Hinz, M.; Bensch, W. Controlling Nucleation and Crystal Growth of a Distinct Polyoxovanadate Cluster: An In Situ Energy Dispersive X-ray Diffraction Study under Solvothermal Conditions. *Chem. - Eur. J.* **2012**, *18*, 15316−15322.
(71) Seidlhofer, B.; Antonova, E.; Wang, J.; Schinkel, D.; Bensch, W. On the Complexity of Crystallization of Thioantimonates: In-situ Energy Dispersive X-ray Diffraction (EDXRD) Studies of the Solvothermal Formation of the Isostructural Thioantimonates [TM(tren)Sb4S7] (TM = Fe, Zn). *Z. Anorg. Allg. Chem.* **2012**, *638*, 2555−2564.

DOI: 10.1021/acs.cgd.7b00450
Cryst. Growth Des. 2017, 17, 3462−3474